**RESEARCH**

# Structural, electric and dielectric studies on $Er^{3+}$/$Yb^{3+}$ co-doped zinc phosphate glasses

I. Soltani[1] · N. Sdiri[1] · K. Horchani-Naifer[1] · M. Férid[1]

**Abstract**

$(42.25-x)Na_2O + (42.25-x)P_2O_5 + 15ZnO + 0.5Er_2O_3 + xYb_2O_3$ with ($x = 0$, 0.5,1, and 1.5%) were processed using the melt quenching method. DSC is used to control the stability of the glass. XRD patterns and Raman analysis were performed to understand the structure of the glass samples. The impedance spectra were analyzed in terms of an equivalent circuit involving bulk resistor ($R_b$) and bulk constant phase elements ($CPE_b$). The ac-conductivity analysis was used to evaluate the effect of increasing the percentage of $Yb_2O_3$ in the glass. Our findings prove that the relaxation time decreases with rising temperature, as well as the average value of the activation energy was in the order of 0.97 eV, which leads to an increase in the ionic conductivity. An improvement in ionic conductivity was demonstrated with the incorporation of $Er_2O_3$ and $Yb_2O_3$ contents.

**Keywords** Phosphate glasses · Rare earths · Raman spectroscopy · Complex impedance

## Introduction

Phosphate glasses are technologically important materials because of their low chemical durability, facility of preparation at low temperatures, low glass transition temperatures, and low optical dispersions. These properties make them useful candidates for fast ion-conducting material and other important applications such as laser hosts and bio-compatible materials [1–4].

The phosphate glasses characteristics can be changed by adding the rare earth ions and transition metals ions into the glassy network [5–7]. Amongst them, the glass containing transition metal ions, which are particularly significant because of their applications as cathode materials in electronics battery materials [8–10]. The dielectric investigation like dielectric constant, dielectric loss, and ac conductivity of phosphate glasses vary with frequency and temperature. Our current study presents the nature and origin of loss taking place in glass and conduction mechanisms and also provides information about the structural features of glasses [11, 12]. It is estimated that transition metal and rare earth ion–doped glasses hold ionic conduction [13]. The introduction of alkali oxides in glass such as $Na_2O$ de-polymerizes the glass structure resulting in the formation of non-bridging oxygen (NBO). The incorporation of alkali ions in the glass matrix produces thermally activated hopping between NBOs [14]. In particular, phosphate glasses are prone to moisture because of the P-O-P link. The phosphate glass incorporated with metal oxides leads to a break in the P-O-P linkages by creating NBO atoms attributable to the depolymerization of the glass network [15, 16]. The great interest in zinc phosphate glasses is continued, thanks to the good chemical durability and the poor processing temperature. These properties lead that it can be co-formed with metallic powder to generate typical zinc phosphate glass/metal composites. Precisely, in the $ZnO-P_2O_5$ glasses, after thermal excitation of electrons from a Zn atom adjacent to an oxygen vacant lattice point, renovating a normal network ion $Zn^{2+}$ gives rise to electronic conduction. The zinc phosphate glass structure consists of $PO_4$-tetrahedral coupled to oxygen polyhedral that contains zinc ions in interstitial positions modifying the glass structure [15, 17]. The aim of the present study was to investigate the electrical and dielectric properties for $Na_2O-P_2O_5-ZnO$ glasses co-doped with rare earth ions ($Er^{3+}$/$Yb^{3+}$) with various concentrations of $Yb_2O_3$ ($x = 0$, 0.5,1, and 1.5%) as a function of frequency (10 Hz to

✉ N. Sdiri
    sdirinasr@yahoo.fr

1   Physical Chemistry Laboratory of Mineral Materials
    and Their Applications, National Center of Research
    in Materials Science, B.P. 73, 8027 Soliman, Tunisia

13 MHz) and in temperature range from 200 to 350 °C. The primary objective is to explore the changes in conduction mechanism that take place by electron hopping from low to the high valence state of ytterbium ions and provides information about the structural features of glasses.

## Experimental details

Phosphate glasses systems $\frac{(84.5-x)}{2}$ $Na_2O + \frac{(84.5-x)}{2}$ $P_2O_5 + 15ZnO + 0.5Er_2O_3 + xYb_2O_3$ with ($x = 0$, $0.5$, $1$, and $1.5\%$) were prepared from the starting chemical constituents $NaH_2PO_4$, $ZnO$, $Er_2O_3$, and $Yb_2O_3$ from high-purity raw materials (99.99%). The corresponding samples are referred to as *NPZ*, *NPZEr05*, *NPZEr05Yb05*, *NPZEr05Yb1*, and *NPZEr05Yb15* respectively, a stoichiometric combination of the basic ingredients were used to make the glasses. To melt the chemicals completely, they were melted in an electric furnace at 900 °C for 2 h at a rate of 10 °C/min. The melt was then poured into a steel mold, which was annealed at 250 °C to minimize thermal expansion. Following the quench, the samples were annealed for 2 h at 250 °C below their glass transition temperature. After that, the samples were allowed to cool at ambient temperature before being polished. After that, the samples have the forms of a disk with a ray ($r = 5.5 \pm 0.01$ mm) and a thickness ($e = 1.7 \pm 0.01$ mm). By using the method of Archimedes (with acetone as immersing liquid), the density ($\rho$) of the current glasses was measured at room temperature [18]. The molar volume ($V_m$) was calculated using the following formula:

$$Vm = \frac{\sum M_i * n_i}{\rho} \tag{1}$$

where $M_i$ is the relative molecular mass of component $i$ and $n_i$ is its molar fraction. The X-ray diffraction patterns of the glasses were recorded on an X'PERT Pro PAN-Analytical diffractometer with CuKα radiation of wavelength (1.5418 Å), with $2\theta$ varying from 3 to 70° with a step size of 0.02°. The glass transition temperature ($T_g$) and crystallization onset temperature ($T_x$) were determined using a MetlerToldo instrument differential scanning calorimetry (DSC) at a heating rate of 10 °C/min from RT to 500 °C. Raman scattering spectra were registered using HORIBA Scientific (lab RAM HR) spectrometer outfitted with laser source (632 nm) and CCD detector. Impedance spectroscopy measurements were carried out using an impedance analyzer (Agilent4294 A) to get complex impedance data, in the range 10-Hz to 13-MHz frequency and temperature ranges 200–350 °C. The electrical conductivity measurements were carried out on samples shaped as plates with two parallel faces.

## Results and discussion

### Density and molar volume

The density ($\rho$) and the molar volume ($V_m$) from all glass samples are listed in Table 1, which increased in parallel with the $Yb_2O_3$ content in the glasses. The increase of the $\rho$ could be explained by considering the higher relative molecular mass of ytterbium oxide as compared to the relative molecular mass of zinc oxide. With the increase of $Yb_2O_3$ content in the glasses, the oxygen content and the molar of the glass volume increase, indicating a more open glass network [19]. On increasing the concentration of $Yb_2O_3$ from $x = 0.5$ to $1.5$, the compactness of the titled glasses structure increases progressively. Meanwhile, $Zn^{2+}$ ions are highly possible to locate as network modifiers instead of as network former to balance the net columbic charges of the structure [20]. In general, structures with a higher degree of disorder result in a broad distribution of both trap sites and migration barriers with the deepest traps likely controlling conduction [20].

### Structural properties

#### XRD analysis

In Fig. 1a, XRD profiles reveal a broad hollow band at $2\theta$ (25–35°), which demonstrates the amorphous nature of the *NPZ*, *NPZEr05*, *NPZEr05Yb05*, and *NPZEr05Yb1* samples, whereas the appearance of significant peaks of the NPZEr05Yb15 glass sample confirms the existence of nanocrystallites, thanks to the increase of ($x$) values

**Table 1** The density ($\rho$), molar volume ($V_m$), bulk resistor ($R_b$), bulk constant phase element ($CPE_b$), and exponent ($n$) for different glass samples at 260 °C

| Samples | $\rho(gcm^{-3})$ | $V_m(cm^3)$ | $R_b 10^4(\Omega)$ | $CPE_b$ $10^{-11}(F. cm^{-2}.s^{n-1})$ | $n$ |
|---|---|---|---|---|---|
| NPZ | 2.70 | 42.19 | 3.59 | 2.02 | 0.93 |
| NPZEr05 | 2.73 | 42.29 | 9.57 | 4.20 | 0.86 |
| NPZEr05Yb05 | 2.76 | 42.23 | 39.57 | 6.15 | 0.84 |
| NPZEr05Yb1 | 2.77 | 42.61 | 105.38 | 13.87 | 0.77 |
| NPZEr05Yb15 | 2.78 | 43.01 | 278.10 | 39.81 | 0.74 |
| **PLA4**[36] | - | - | $0.724 \ 10^{-3}$ | 0.44 | 0.96 |

**Fig. 1** **a** XRD patterns of different phosphate glasses, **b, c** XRD patterns of the studied glass NPZEr05Yb15 around $2\theta = 26.2°$ at room temperature
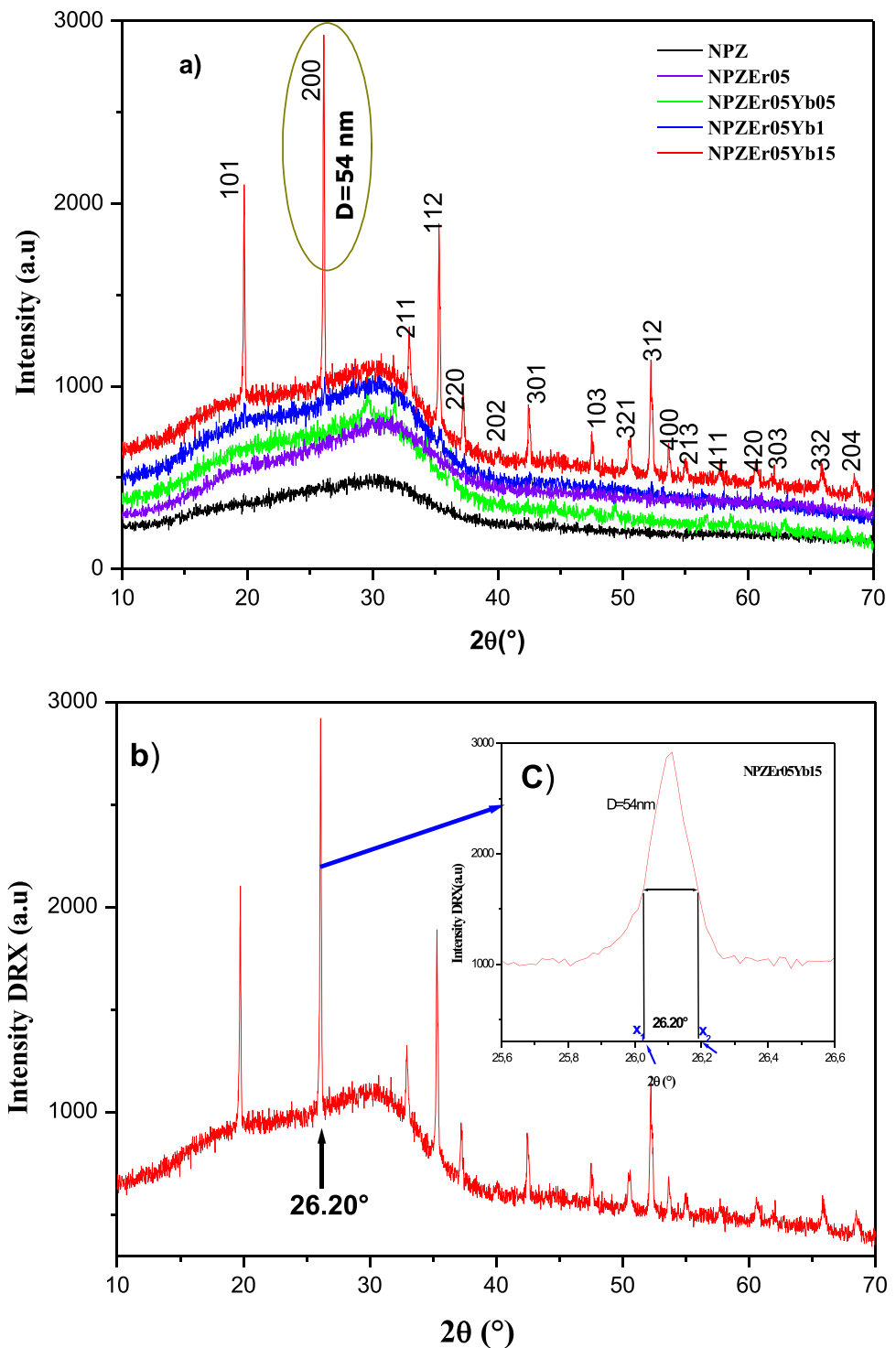


of $Yb_2O_3$ from ($x = 0.5$) to ($x = 1.5$). The diffraction peaks can be caused by the increase of crystallite size. The XRD pattern is comprised of small bands originating from a wide halo at $2\theta = 26.2°$, indicating the existence of small crystallites in an amorphous glass. This crystalline phase attributed to tetragonal phosphate ytterbium ($YbPO_4$) with space group $I41/amd$, similar lattice parameter values ($a = 6.809$ Å; $b = 6.809$ Å; $c = 5.963$ Å and $Z = 4$), with diffraction peaks indexed according to JCPDF card # 45–530. Figure 1b displays the evolution of the intense peak with the ytterbium amount. This peak is detailed in Fig. 1c. The average crystallite size for the $YbPO_4$ phase was computed using the Scherer formula [21, 22]:

$$D = \frac{0.89\lambda}{\beta cos\theta} \qquad (2)$$

where $D$ represents the crystallite size, $\lambda$ the wavelength of CuK$\alpha$1 radiation, $\theta = (13.1 \pm 0.1)°$ the Bragg diffraction angle of the XRD peak, and $\beta$ is the full width at half maximum (FWHM). The average crystallite sizes of NPZ-Er05Yb15 glass samples were calculated to be 54 nm. Additionally, we estimated the average particle size D uncertainties that have been given by:

$$\Delta D = D.\frac{\Delta\beta}{(\beta} + \frac{\Delta(cos\theta)}{cos\theta)} \qquad (3)$$

where $\Delta\beta = \pm 0.01°$ and $\Delta (cos\theta) = 0.001$ [22]; the uncertainties ($\Delta$D) of the crystallite have to be 2.81 nm.

### Thermal analysis

Figure 2 shows the DSC of all glass samples at a heating rate of 10 °C/min. The glass transition temperature ($T_g$), crystallization onset temperature ($T_x$), and thermal stability $\Delta T = T_x\text{-}T_g$ are tabulated in Table 2. From the literature [23], it is found that, if the value of $\Delta T$

**Table 2** Thermal parameters of NPZ and NPZEr05 glass samples

| Glass | $T_g$(°C) | $T_x$(°C) | $\Delta T = T_x\text{-}Tg$(°C) |
|---|---|---|---|
| NPZ | 275 | 378 | 103 |
| NPZEr05 | 277 | 388 | 112 |

is higher than 100 °C, the glass can be considered as thermally stable. From the value of $\Delta T$, it is found that for the samples the value of $\Delta T$ is higher than 100 °C and increase with adding the $Er_2O_3$ content. From the data, it is found that phosphate glasses containing $Er_2O_3$ are thermally more stable than the phosphate glasses without $Er_2O_3$.

### Raman analysis

The structural modifications of phosphate glasses induced by increasing of $Yb_2O_3$ content is exhibited in Fig. 3. Raman spectra of the present glass were analyzed according to the assignments of Raman bands for different phosphate glasses [24–26]. The Raman spectrum exhibits seven bands at 349 cm$^{-1}$, 554 cm$^{-1}$, 690 cm$^{-1}$, 903 cm$^{-1}$, 1030 cm$^{-1}$, 1051 cm$^{-1}$, and 1275 cm$^{-1}$.The
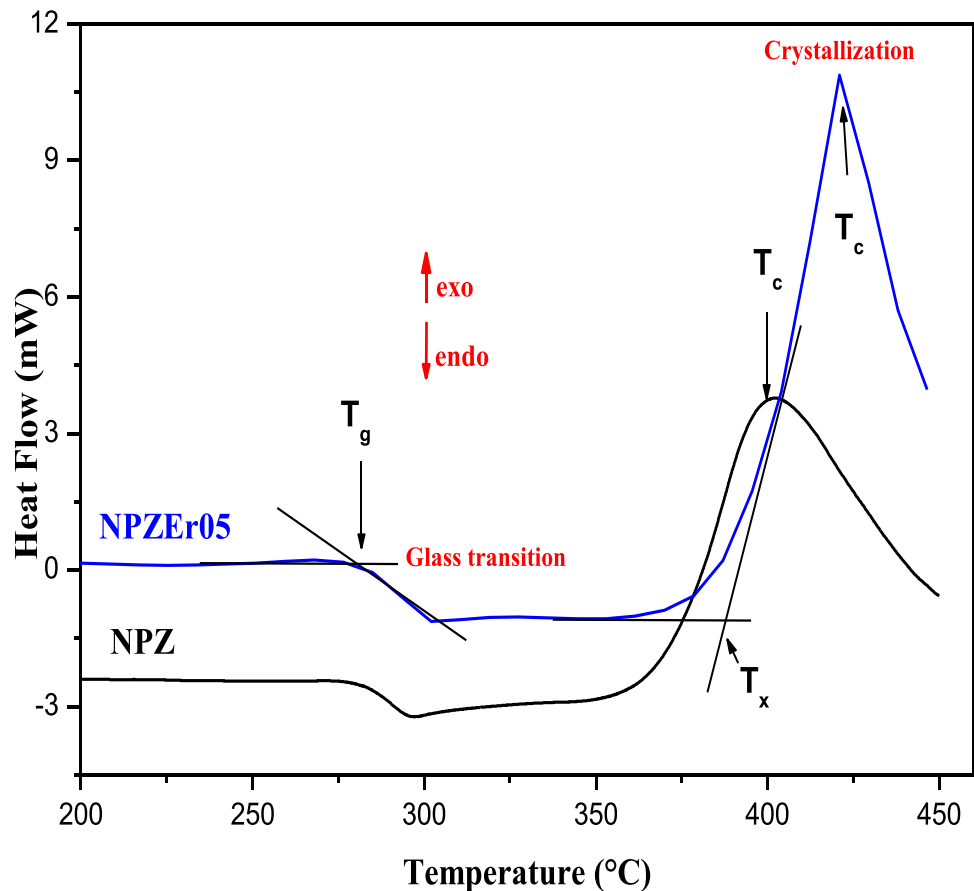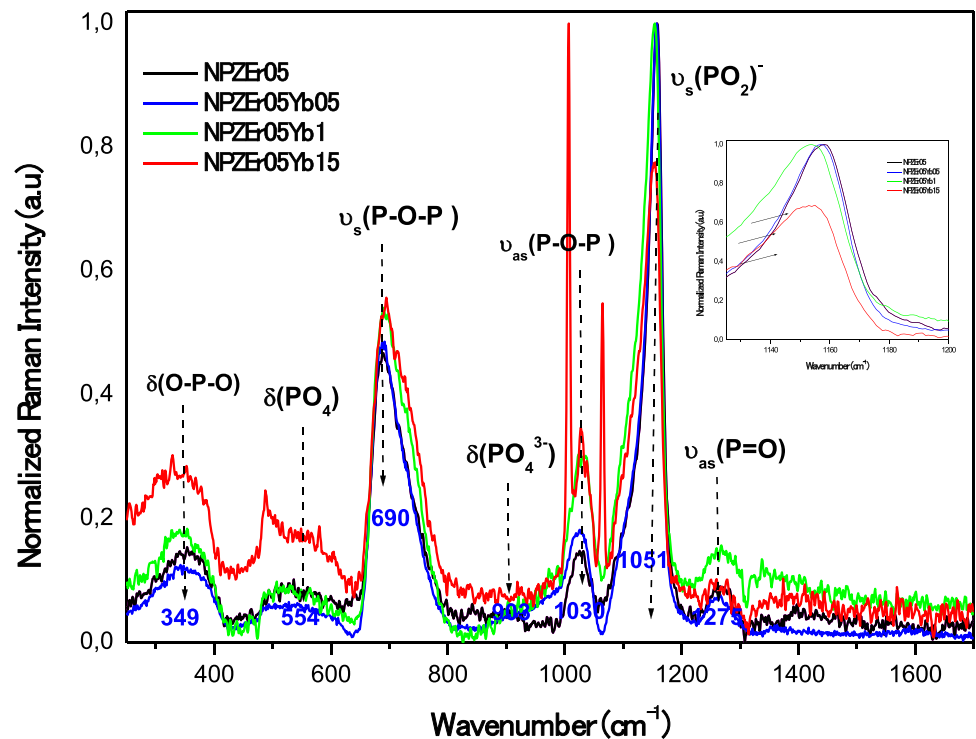
**Fig. 2** DSC thermogram of the NPZ and NPZEr05 samples

**Fig. 3** Raman spectrum of different phosphate glass samples



band at 349 cm$^{-1}$ is due to δ (O–P–O) [27]. The peak at 554 cm$^{-1}$ is due to δ (PO$_4$) tetrahedron [28]. The band at 690 cm$^{-1}$ is due to P–O–P (bridging oxygen) stretching modes, the peak at 903 cm$^{-1}$ is attributed to the δ(PO$_4$$^{3-}$).The band at 1030 cm$^{-1}$is due to anti-symmetric vibration $\upsilon_{as}$(P–O–P), and a strong signal at 1051 cm$^{-1}$ is due to the $\upsilon_s$(PO$_2$)$^-$, the most observed band at 1275 cm$^{-1}$ is due to the (PO$_2$) anti-symmetric vibration ($\upsilon_{as}$P = O). The same modes are detected with variations in strength and location based on the Raman spectra. With increasing of Yb$_2$O$_3$ content, the intensity of the band around 1030 cm$^{-1}$ increases while $x$ values increase from $x = 0.5$ to $x = 1.5$ mol%. These modifications indicate that the phosphate-based glass was depolymerized by modifying cations (Na$^+$).The addition of rare earth cations depolymerizes the phosphate-based glass[29], by breaking the P–O–P bonds, leading to non-bridging oxygen (–P–O–). On the other hand, it was found that the most intense peak around 690 cm$^{-1}$ shifted towards a higher wave number value. This shift is due to internal strain developed by the substitution of Zn$^{2+}$ by Er$^{3+}$/Yb$^{3+}$dopant ions [30–33]. Also Fig. 3 shows the appearance of fine and intense peaks of the NPZEr05Yb15 glass sample compared to other samples; the peaks can be caused by the increase of crystallite size, revealing the existence of certain nanocrystallites in this material.

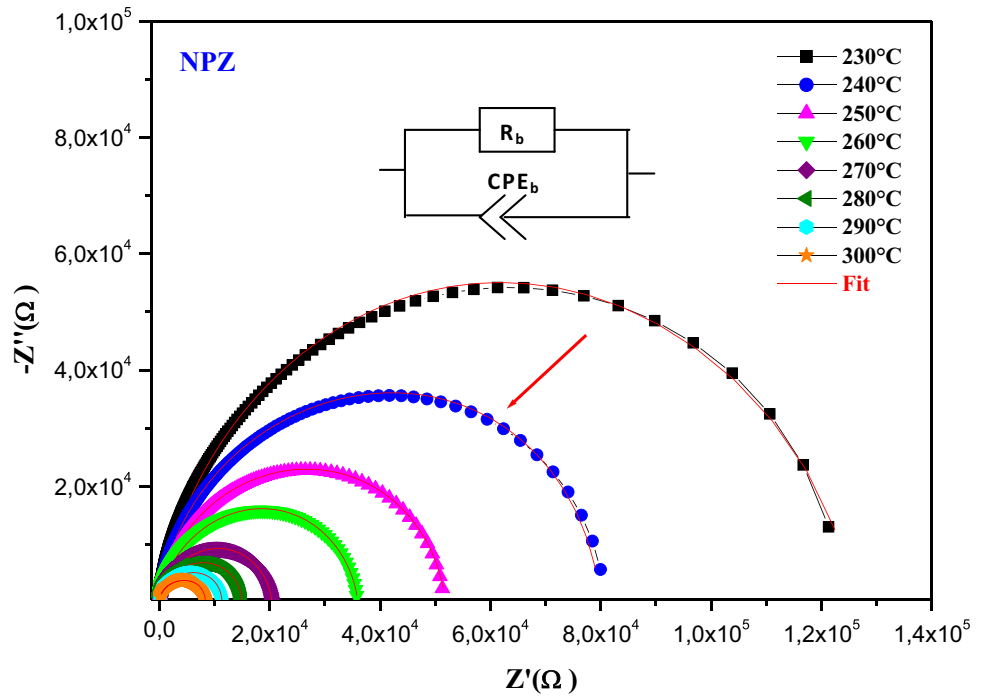## Electrical and dielectric measurements

### Impedance spectroscopy

Figure 4 shows the complex impedance plots of the NPZ glass sample, which identify the electric movement in the glass at different temperatures (230–300 °C). The absence of a second arc in the complicated plane plots at various temperatures indicates that the dielectric relaxation is exclusively a bulk phenomenon in these materials [34]. Therefore, the proposed equivalent circuit is formed by a bulk resistor (R$_b$), in parallel to a bulk constant-phase element (CPE$_b$). The experimental data are compared to a theoretical curve fitting, a good agreement between experimental and theoretical results. These semicircles are typically depressed, with their centers lying below the Z′ axis in all cases, indicating non-Debye relaxation [35, 36]. It is found that with rising temperature, the curves diminished and moved to a higher frequency, this is explained by the enhancement in conductivity [37, 38], also shows a thermally activated conduction mechanism[39]. The total impedance of the equivalent circuit is given by:

$$Z^* = Z' + jZ'' = \left(\frac{1}{R_b} + \frac{1}{Z_{CPE_b}}\right)^{-1} \tag{4}$$

Z′ and Z" are the real and imaginary components of impedance.

**Fig. 4** Complex impedance plot (Z',-Z'') at different temperatures for the NPZ glass sample with the equivalent circuit diagram, where $CPE_b$ is the bulk capacitance and $R_b$ is the bulk resistance



The impedance of the $CPE_b$ is defined via [40]:

$$Z^*_{CPE_b} = \frac{1}{A_0(jw)^n} \qquad (5)$$

where $j$ represents the imaginary unit ($j^2 = -1$) and $\omega$ represents angular frequency ($\omega = 2\pi f$, f the frequency), $A_0$ a constant independent of frequency and in F.cm F.cm$^{-2}$. s$^{n-1}$ [41], and $n$ is an exponent index which is a measure of arc depression ranging between zero and unity. When $n = 1$, Eq. (4) gives the impedance of a capacitor, where $A_0 = C$; the bulk resistance $R_b$ is the cross of the axis with the impedance curve. The diagrams of Nyquist plots are fitted with the ORIGIN6.0 program based on relationships (6) and (7):

$$Z' = \frac{R_b(1 + R_b(A_0)\omega^n \cos(\frac{n\pi}{2}))}{1 + 2R_b(A_0)\omega^n \cos(\frac{n\pi}{2}) + (R_b(A_0)\omega^n)^2} \qquad (6)$$

$$Z'' = -\frac{(R_b)^2(A_0)\omega^n \sin(\frac{n\pi}{2})}{1 + 2R_b(A_0)\omega^n \cos(\frac{n\pi}{2}) + (R_b(A_0)\omega^n)^2} \qquad (7)$$

Figure 5 shows the impedance plot for all glass samples at 260 °C, which exhibited the same behavior. The value of $R_b$ and $CPE_b$ of parallel RC circuits for different glass samples are listed in Table 1 and compared with other glasses [36]. It is observed that the incorporation of $Er_2O_3$ and $Yb_2O_3$ contents increased the $CPE_b$ in the glass systems and decreased the value of $n$. As a result, the glass network works like a capacitor, within the experimental frequency range (10 Hz to 13 MHz). Z'' and Z' are plotted against frequency to demonstrate the frequency-dependent conductivity behavior of the NPZEr05 glass between 230 and 280 °C, as shown in Fig. 6. It can be shown that as the frequency rises, the real component of the impedance Z' decreases. With increasing frequency and temperature, this drop in Z' indicates an increase in the ac conductivity of the material. The Z' values fuse at higher frequencies for all temperatures, due to the release of space charge and a decrease in the material's potential barrier [42]. The graphs indicate that the Z'' values reach a maximum peak Z'' max and that the Z'' at each temperature displays a relaxation peak whose peak frequency ($f_{max}$) moves toward higher frequencies with increasing temperature and follows the Arrhenius equation, implying that the ion transport mechanism is changing [39].The relaxation time of samples was estimated using the relation $\tau = 1/\omega_{max} = 1/2\pi f_{max}$, where $\omega_{max}$ correspond to the maximum value of Z'' determined through the plots in Fig. 6. The plot of relaxation time against (1000/T) for the NPZEr05glass sample is shown in Fig. 7. It is found that the relaxation time obeys the Arrhenius law [43]:

$$\tau_r = \tau_0 \exp(E \downarrow re/(K \downarrow BT)) \qquad (8)$$

where $E_{re}$ is the energy of dipolar relaxation. In Fig. 7, the energy of 0.81 eV is derived by drawing a curve between relaxation time and temperature. This implies that the relaxation is temperature-dependent and that there is not a single relaxation time. It is obvious that frequency and temperature affect conductivity may be related to the hopping process of

**Fig. 5** Experimental and theoretical impedance diagrams of the NPZ, NPZEr05, NPZ-Er05Yb05, NPZEr05Yb1, and NPZEr05Yb15 glasses with inset the corresponding equivalent circuit at $T=260°C$
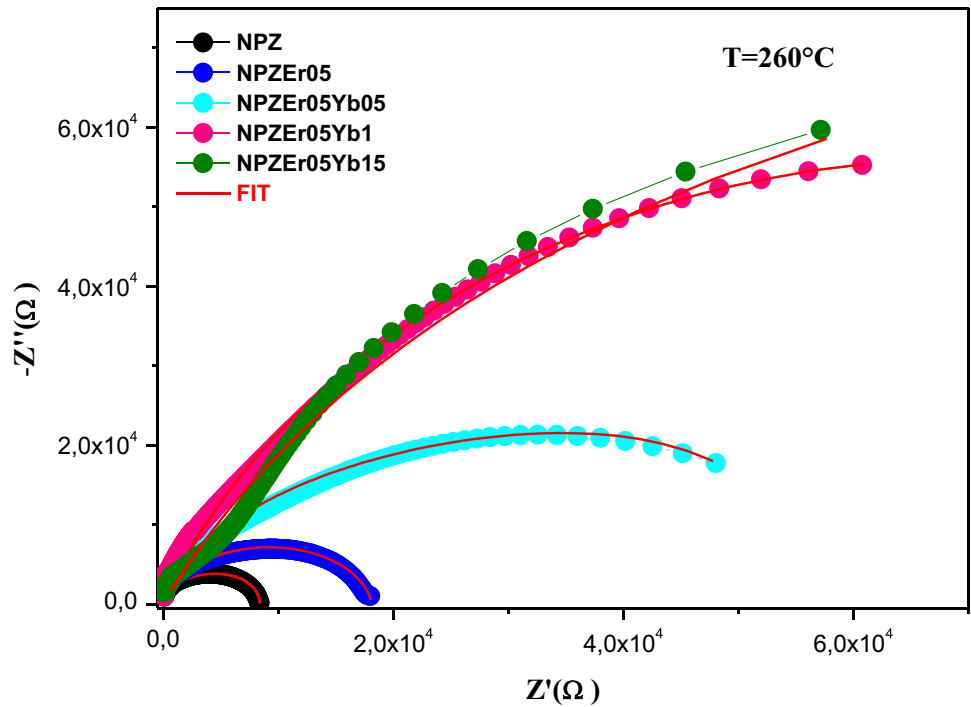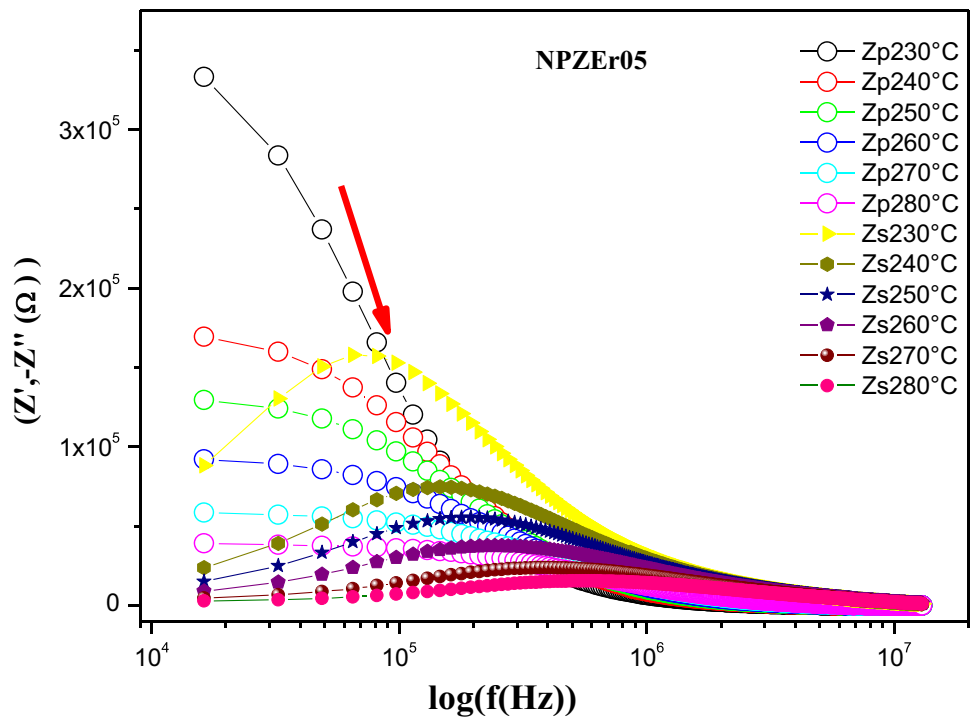


**Fig. 6** Variation of imaginary ($Z''$) and real ($Z'$) part of impedance of NPZEr05 with frequency at different temperatures



charge carrier transport [44]. The ac conductivity is computed from the data of complex impedance values [45]:

$$\sigma_{ac} = \frac{e}{\pi r^2} \frac{Z'}{\left(Z'^2 + Z''^2\right)} \tag{9}$$

The ac conductivity ($\sigma_{ac}$) of NPZEr05 glass versus frequency at different temperatures is shown in Fig. 8.The $\sigma_{ac}$ of all the glass samples is similar, with the slope changing to higher values as the frequency increases. As we can see in Fig. 8, the dc conductivity sample is frequency-independent at low frequencies, but it corresponds to the dispersion area at higher frequencies, where the conductivity

**Fig. 7** Variation of relaxation time Ln ($\tau$) of NPZEr05 with inverse of temperature 1000/T
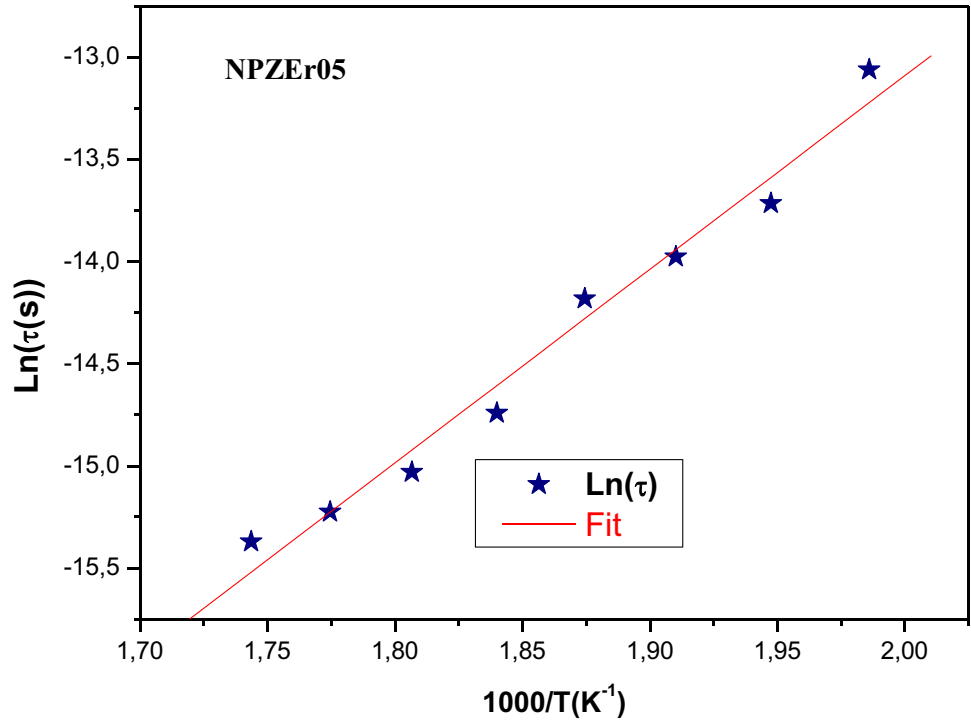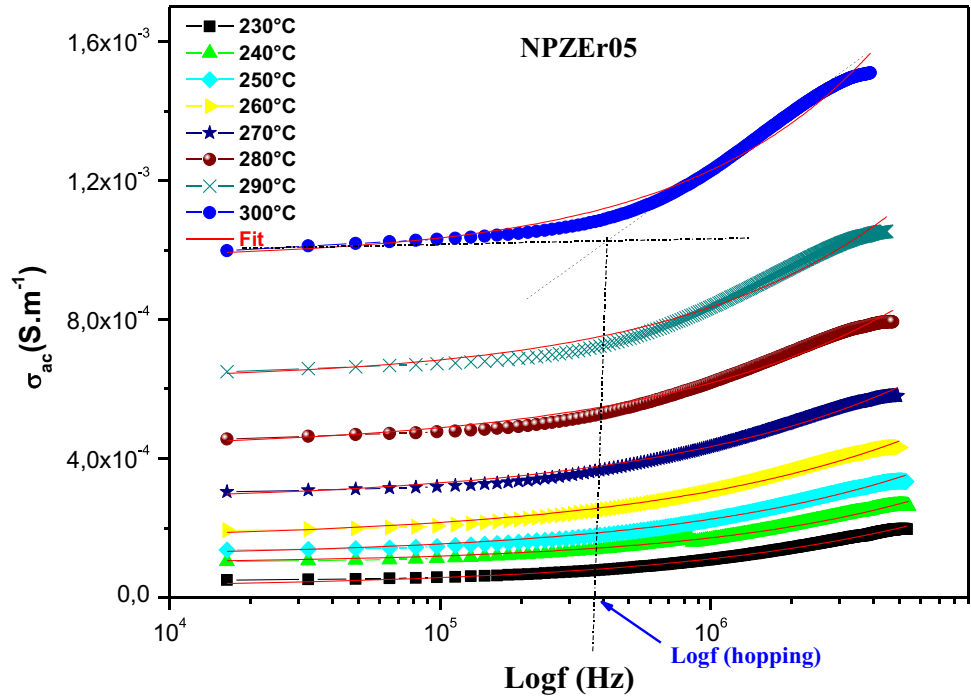


**Fig. 8** Variation of the ac conductivity ($\sigma$ac) of NPZEr05 glass versus frequency at different temperatures



changes to higher frequencies with temperature. The conductivity relaxation phenomena were emphasized by the $\sigma_{ac}$ change with frequency. Jonscher's power law of $\sigma_{ac}$ is used to investigate the process of conductivity dispersion [46, 47]:

$$\sigma_{ac} = \sigma + A(f)^{s1} + A_2(f)^{s2} \tag{10}$$

where $\sigma_{dc}$ is the dc conductivity in a particular range of temperature and frequency and the terms $s_1$ and $s_2$ are exponents corresponding to low- and high-frequency region and varies from 0 to 1 ($0 \leq s_1, s_2 \leq 1$) [48, 49]. $A_1$ and $A_2$

are constants relating to the low- and high-frequency areas, respectively, slopes traced to the experimental data in the low- and high-frequency regions will cross at a point, and the frequency reacting to this point is termed relaxing frequency[50]. The curves overlapped near the conclusion of the high frequency, indicating the potential of the presence of space charges [51]. This is a fair as assumption because the space charge effect disappears at higher temperatures and frequencies, implying the presence of a hopping mechanism between the allowed sites [52, 53].

Figure 9 shows the variation of the exponent factors, $s_1$ and $s_2$ as a function of the temperature of the NPZEr05glass sample. The exponent values of $s_1$ and $s_2$ lie in the range 0.44–0.6; this is explicated by the correlation motion which indicates a preference on the part of ions that has hopped away to return to its point of departure[45]. It is observed in Fig. 9 that with increasing temperature, exponents' $s_1$ and $s_2$ decrease in the range 240–260 °C and increase in the range 260–300 °C. It is known that a study of the variation of $s$ with temperature can throw light on the conduction mechanism [54, 55]. If $s_1$ and $s_2$ decrease with the temperature, this behavior was anticipated earlier by the correlated barrier hopping (CBH) model, which depicts charge carriers hopping between sites rather than tunneling through the potential barrier separating them [56]. In this investigation, the variation of $s_1$ and $s_2$ indicates the possibility of an overlapping large polaron tunneling mechanism (OLPT). In this model, long has suggested a polaron tunnel mechanism where polaron energy comes from polarization changes in the deformed lattice [57]. According to the CBH model, the exponent s parameter is written as follows:

$$\sigma_{dc} = \sigma_0 \exp(-E_a/k_B T) \tag{11}$$

where $k_B$ is Boltzmann constant, $W_M$ is optical band gap, and $T$ is the absolute temperature. With increasing temperature, the thermal motion increases and the ability to polarize the ions locally in the network reduces. If $s_1$ and $s_2$ increase with the temperature, the small polaron (SP) model indicates that the conduction is predominant [58]. Furthermore, if the polarizability of the concerned material is dependent on the energy barrier for a simple hopping operation between two sites, change of the exponents' $s_1$ and $s_2$ can be predicted [59]. In general, the power law exponents' $s_1$ and $s_2$ for ionic conductivity may be between 0.5 and 1, indicating excellent long-range routes and diffusion-limited hopping [60]. In Fig. 10, we represent the variation of the hopping time for the NPZ and NPZEr05 with different temperatures. The $\tau$ hopping increases slowly with increasing temperature up to 265 °C over 270 °C then decreases with the increase of the temperature, which suggests that the incorporation of $Er^{3+}$ions in the glass matrix speed up the transition between the sites that lead the increase of the conductivity. This decrease may be due also to the internal strain developed by the substitution of $Zn^{2+}$ by $Er^{3+}$ions [32, 61]. According to the Arrhenius equation, dc conductivity may be well characterized by the activation type of temperature dependency:

$$\sigma_{dc} = \sigma_0 \exp(-E_a/k_B T) \tag{12}$$

where $E_a$ is the activation energy, $\sigma_0$ is the pre-exponential factor, $k_B$ is the Boltzmann constant, and $T$ is temperature. Figure 11 shows the Arrhenius plots of dc conductivity of all glasses. The values of $\sigma_{dc}$ and $E_a$ are listed in Table 3.



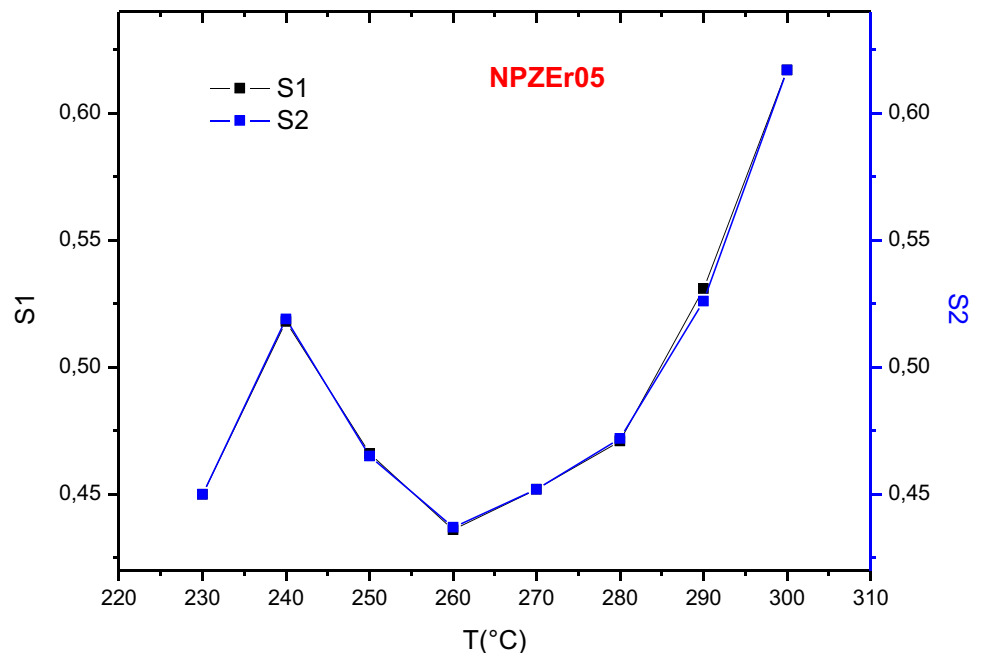**Fig. 9** Variation of the exponent parameters $S_1$ and $S_2$ with temperature for the NPZEr05 sample

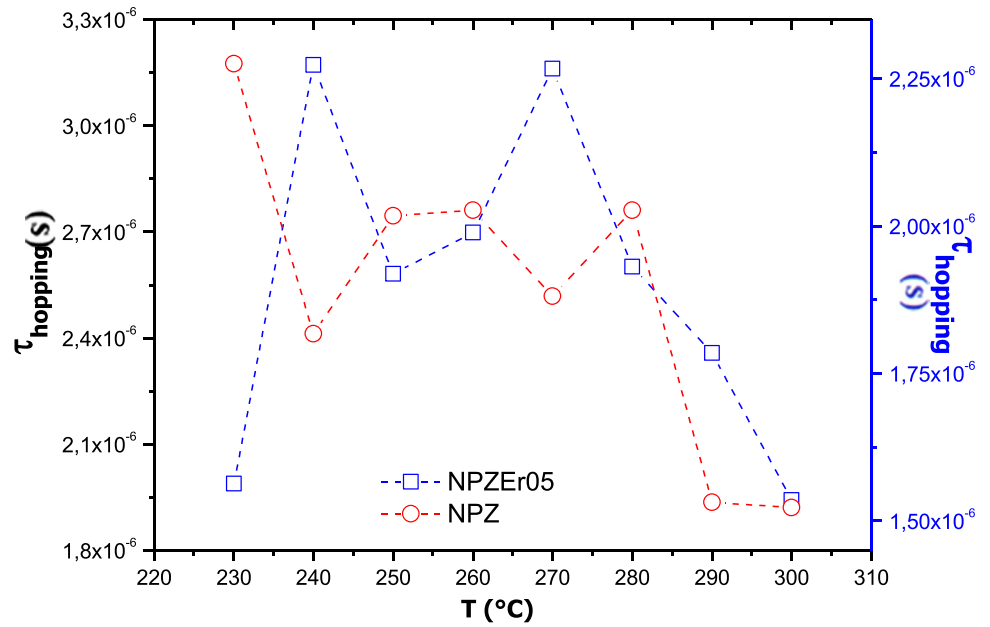**Fig. 10** Variation of the hopping time (τ hopping) for NPZ and NPZEr05 at different temperatures



**Fig. 11** Arrhenius relation of Ln(σdcT) versus 1000/T for NPZ, NPZEr05, NPZEr05Yb05, NPZEr05Yb1, and NPZEr05Yb15 glasses
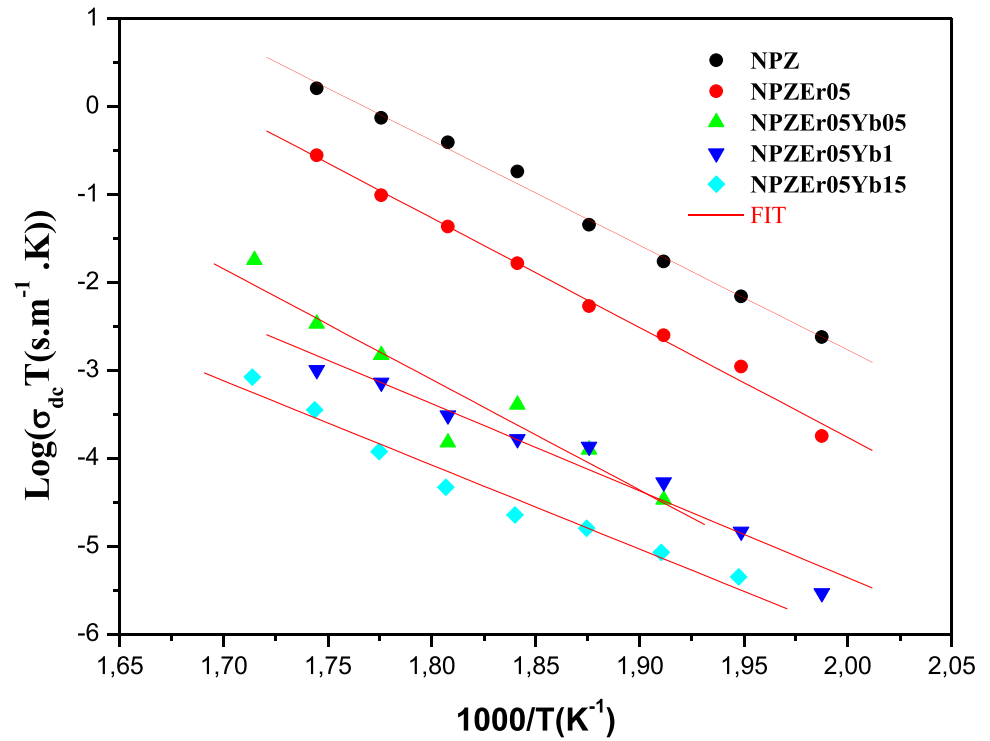


**Table 3** Values of the dc conductivity (σ$_{dc}$) and activation energy(E$_a$) for different samples

| Samples | NPZ | NPZEr05 | NPZEr05Yb05 | NPZEr05Yb1 | NPZEr05Yb15 | *PLA4*[36] |
|---|---|---|---|---|---|---|
| σ$_{dc}$(S m$^{-1}$)à | 21.4 E-4 | 1E-3 | 1.473 E-4 | 8.743 E-5 | 5.743 E-5 | 5.20 E-6 |
| E$_a$(ev) | 1.02 | 1.07 | 1.08 | 0.86 | 0.82 | - |

It is clear from Fig. 11 that the $\sigma_{dc}$ progressively increases with the incorporation of $Er_2O_3$ and $Yb_2O_3$ contents in the structure. The conductivity increases by two orders of magnitude when $Yb_2O_3$ content is raised from 0.5 to 1.5 mol%. The structural alterations in the phosphate glass network are expected to cause such behavior. This procedure is repeated until the glass-forming oxides have used up all of the modifier's oxide ions ($P_2O_5$). With the opening of the network, non-bridging oxygen is produced, which is expected to enable increased $Na^+$ ion mobility, leading to an increase in conductivity. In addition, when the temperature raises, the conductivity rises, resulting in a thermally triggered conduction mechanism.

The presence of ZnO may be thought of as a modifier: $ZnO \rightarrow Zn^{2+} + O^{2-}$. The $O^{2-}$ will participate in the depolymerization of the network, resulting in the creation of the metaphosphate network, which has been further deteriorated. As a result, the conductivity should rise gradually. The ion activation hop's energy is in the range of 0.82 to 1.02 eV. The activation energy decreases with $Yb_2O_3$ mol%, as shown in Table 3. This is due to the partial opening of the 3D network structure, which reduces the average chain length by breaking the oxygen bonds that create bridges between the corners of the $PO_4$ tetrahedron, allowing the $Na^+$ ion to move more easily [13]. The NPZEr05Yb05 glass sample has the greatest activation energy (Ea) value of 1.08, indicating that adding $Na^+$ to the former ($P_2O_5$) not only changes the network by producing non-bridging oxygen (NBO) in the structure but also produces anionic sites with different binding energies of the alkali ions. The ionic conductivity, like crystal conductivity, may be represented by ionic defect migration [62]. The low value of $E_a$ is equal to 0.82 obtained for the NPZEr05Yb05 glass sample, so the increase of the $Yb_2O_3$ content improves the ionic conductivity, the result is explained by the presence of nanometers grain size confirmed by XRD diffraction. These differences are explained by structural alterations that occur as a result of compositional changes in the phosphate glasses network.

## Dielectric properties

### Permittivity and loss studies

The complex permittivity $\varepsilon^*(\omega)$ can be expressed as a complex number [52]:

$$\varepsilon^*(\omega) = \varepsilon'(\omega) - j\varepsilon''(\omega) = \frac{1}{j\omega C_0(Z' + jZ')} \tag{13}$$

$$\varepsilon' = -\frac{Z''}{\omega C_0(Z'^2 + jZ''^2)} \tag{14}$$

$$\varepsilon'' = -\frac{Z'}{\omega C_0(Z'^2 + jZ''^2)} \tag{15}$$

where $\varepsilon'(\omega)$ is the real part of permittivity which represents the polarizability of the material and $\varepsilon''(\omega)$ is the



**Fig. 12** The frequency dependence curves of dielectric constant $\varepsilon'(\omega)$ of NPZ glass at different temperatures
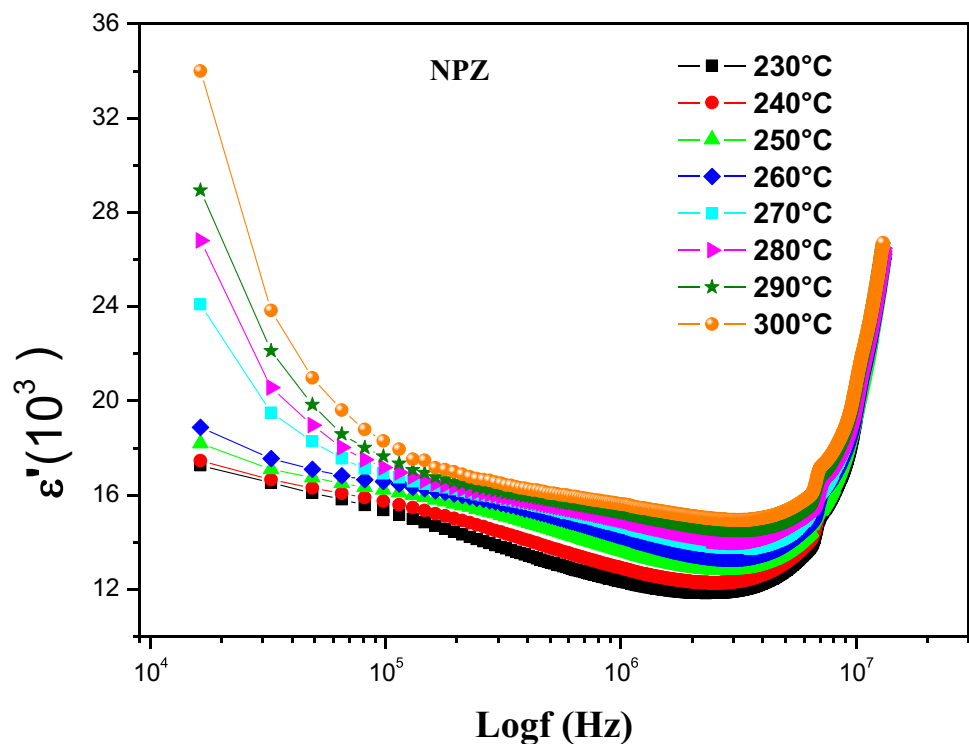
**Fig. 13** The frequency dependence curves of dielectric constant $\varepsilon'(\omega)$
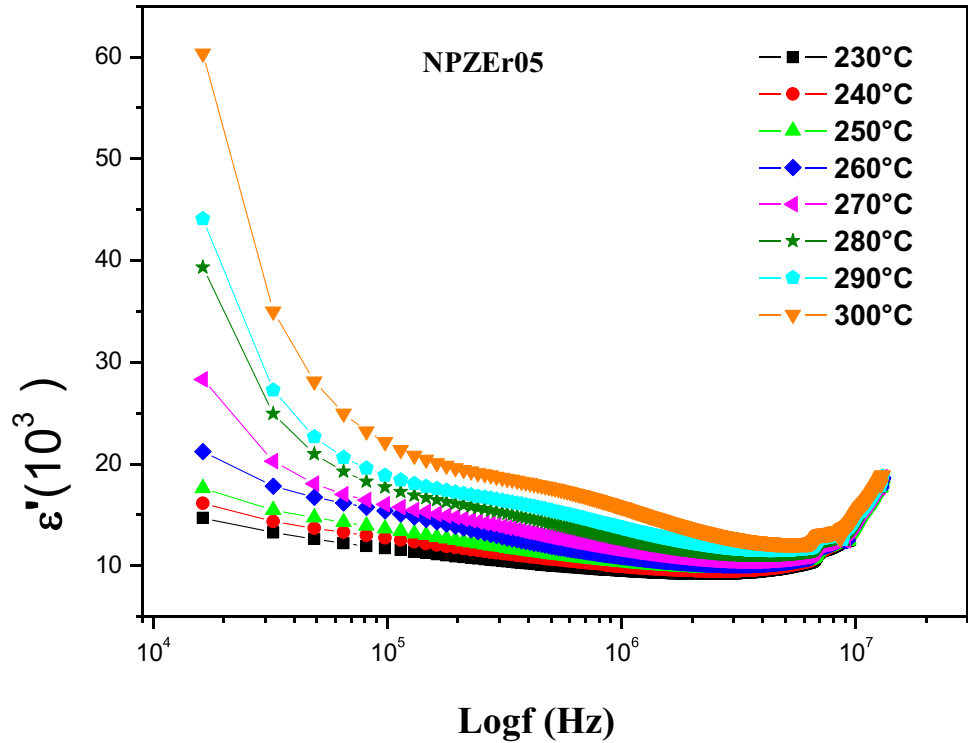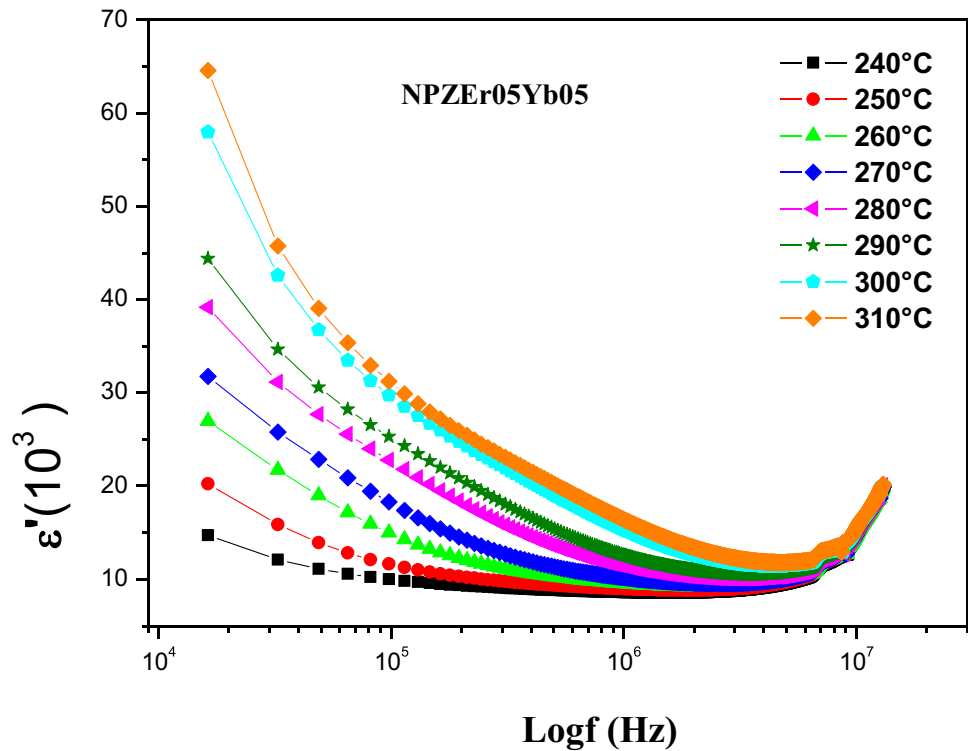


**Fig. 14** The frequency dependence curves of dielectric constant $\varepsilon'(\omega)$ of NPZEr05Yb05 glass at different temperatures



imaginary part representing the energy loss [63]. $C_0 = \varepsilon_0 A/e$ is the capacitance of the void ($\varepsilon_0$ is the permittivity of the vacuum ($8.854 \cdot 10^{-12}$ F m$^{-1}$), $A$ is the cross-sectional area of the flat surface of the pellet and $e$ is its thickness (1.70 mm).

Figures 12, 13, and 14 illustrate respectively the temperature dependence of $\varepsilon'(\omega)$ for NPZ, NPZEr05, and NPZEr05Yb05 samples at various temperatures with logarithmic frequency. In all frequency ranges, it is clear that the

three samples have the highest values of $\varepsilon'(\omega)$, compared to the other samples [64–66]. At low frequencies, in Figs.12, 13, and 14, the values of $\varepsilon'(\omega)$ (300 °C) are equal to $34.10^3$ $Fm^{-1}$, $60.10^3$ $Fm^{-1}$, and $65.10^3$ $Fm^{-1}$ for NPZ, NPZEr05, and NPZEr05Yb05, respectively. We notice that $\varepsilon'(\omega)$ rises with the addition of $Er_2O_3$ and $Yb_2O_3$ and approaches a low-frequency plateau, which we attribute to the polarization effects of mobile ion long-range hopping concerning the stationary glass matrix [67]. As a result, the growing trend is attributed to an increase in dipolar density, which enhances polarization. Moreover, obvious dispersions were detected from the $\varepsilon'(\omega)$ spectra, which is related to the application field that promotes electron hopping between two different locations in glasses. We may infer that $Er^{3+}$ is simpler to polarize since it is trivalent ($Er^{3+}$) and has a high polarity, which leads to the formation of non-bridging oxygen. As a result, the production of NBO raises the dielectric constant of NPZEr05. The incorporation of $Er_2O_3$ and $Yb_2O_3$ can also greatly improve the $\varepsilon'(\omega)$ spectra. At higher frequencies, the $\varepsilon'(\omega)$ approaches a constant value ($27.10^3$ $F\,m^{-1}$) in all temperature ranges for NPZ, NPZEr05, and NPZEr05Yb05, which is caused by fast polarization events in the glasses under applied field [68]. For the present series of glasses, $\varepsilon'(\omega)$ it is very important at a higher frequency and no obvious dispersions were detected from the $\varepsilon'(\omega)$ spectra.

Figure 15 shows the variation of dielectric loss $\varepsilon''(\omega)$ with logarithmic frequency for all glass samples at 300 °C. It can be seen that $\varepsilon''(\omega)$ decreases gradually with the increase in frequency. Initially, the $\varepsilon''(\omega)$ decreases up to about $10^5$ Hz, and after that approaches a constant value ($\varepsilon''_{\infty}$), this is

explained by the fast polarization processes that occur in the glasses under applied field conditions [68]. Charge carriers accumulated at the electrode–electrolyte interface generated dipoles that oscillate with the frequency of the applied field. These oscillations may not be in phase with the electric field, resulting in a reduction in the dielectric loss factor at higher frequencies [69]. Dielectric loss varies due to energy dissipation, ionic transport, and charge polarization. The factor which is defined as phase difference coming from the loss energy within the sample is the dielectric loss factor, $\tan(\delta)$ at different frequencies expressed by [70]:

$$\tan(\delta) = \frac{Z'}{Z''} = \frac{\varepsilon''}{\varepsilon'} \tag{16}$$

Figure 16 shows the variation of $\tan(\delta)$ and quality factor $\frac{1}{(Q=\tan\delta)}$ with the logarithmic frequency of NPZ glass at different temperatures. The dielectric loss ($\tan(\delta)$) is found to be significant at low frequencies, and then declines until it reaches around 105 Hz when the quality factor (Q) approaches a constant value. This might be owing to the faster reaction of the active component than the reactive component [66]. The low dielectric loss value shows that the glasses manufactured are of excellent quality [71]. Additionally, $\tan(\delta)$ increases with increasing temperature; this is owing to the contribution of both ion jump and conduction loss, as well as the existence of all forms of polarization, including electronic, ionic, orientation, and space charge polarization [35]. The purity and quality of the sample will determine the space charge polarization. It has a strong



**Fig. 15** The frequency dependence curves of conduction loss ε "(ω) at $T = 300$ °C for NPZ, NPZEr05, NPZEr05Yb05, NPZEr05Yb1, and NPZEr05Yb15 glasses
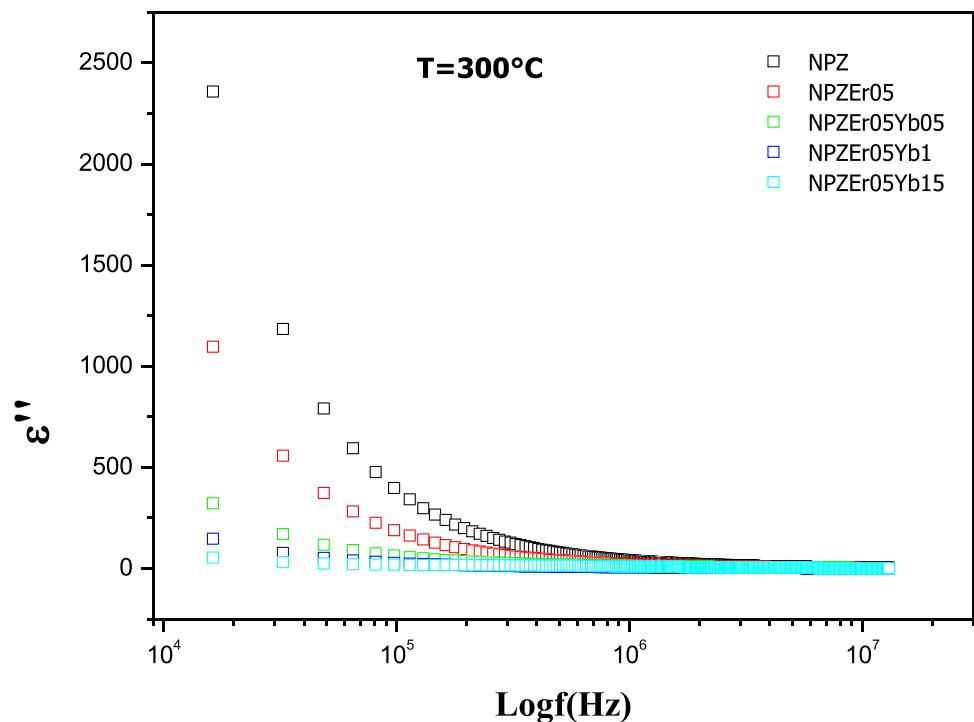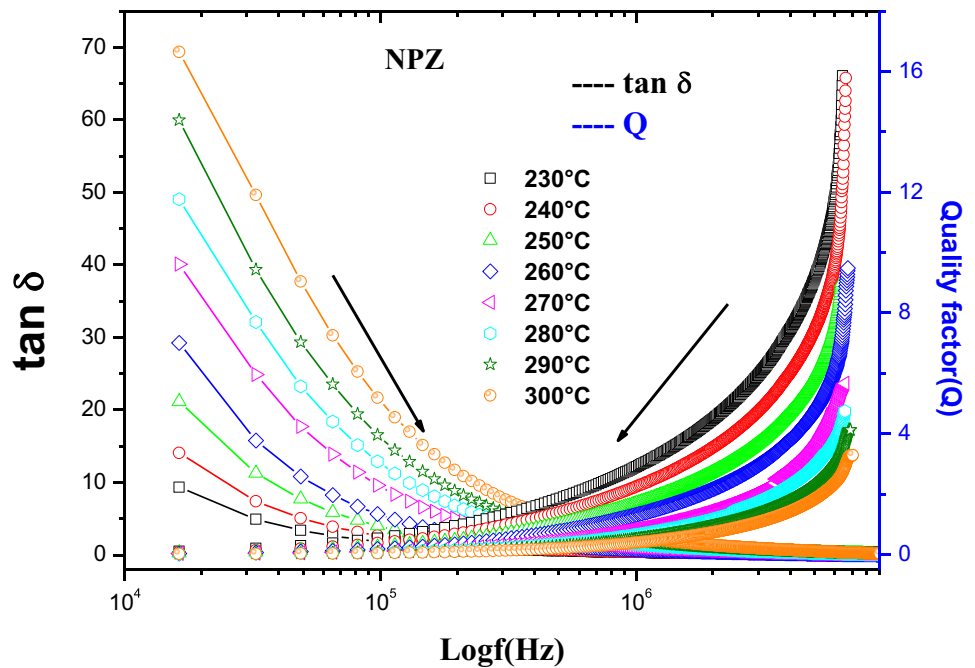
**Fig. 16** Variation of loss tan(δ) and quality factor, *Q* values, versus frequency for NPZ glass at different temperatures



impact at high temperatures and is visible in the low-frequency range [72]. Tan(δ) reduces at higher frequencies until it reaches a constant value at which the quality factor (Q) increases and is determined to be greater. As the temperature rises, the factor (Q) lowers as well. As the frequency of the applied field grows, the ions become more unable to respond to it, and the loss factor decreases, which can be connected to a decrease in matrix ions diffusion with increasing frequency [73]. The low dielectric loss of the samples at higher frequencies is crucial in the use of nonlinear optical materials [74].

## Electric modulus analysis

The electric modulus is an alternative way of determining the relationship between conductivity and mobile ion relaxation in these glasses. The modulus representation was shown to be beneficial in analyzing the relaxation characteristics of both vitreous ionic conductors [75]. The definition of the dielectric modulus is expressed as:

$$M^* = M'(\omega) + j\, M''(\omega) \qquad (17)$$

where $M'(\omega) = \omega C_0 Z''$ and $M''(\omega) = \omega C_0 Z'$. The frequency dependence of the real $M'(\omega)$ and imaginary $M''(\omega)$ parts of the electric modulus for NPZ glass at different temperatures is shown in Figs. 17 and 18. The $M'(\omega)$ and $M''(\omega)$ approach to 0 at low frequencies, suggesting that the electrode polarization phenomena contributes very little to M*, also indicating that the absence

of a restoring force for mobile alkali ions generated by an electric field. The relaxation process associated with point defects, such as trapping and de-trapping of electrons in deep traps in the bulk or in depletion layer areas, causes $M'(\omega)$ and $M''(\omega)$ to rise with increasing frequency and exhibit a maximum value [76]. At different temperatures, the $M''(\omega)$ peak height is essentially equal, and it shifts to a higher frequency as the temperature rises [77]. This may be related to the dispersion of attempt frequencies to overcome the potential barrier [38, 78].

Figures 19 and 20 illustrate respectively the frequency dependence of $M'(\omega)$ and $M''(\omega)$ at 300 °C for all glass samples. The $M''(\omega)$ spectrum in Fig. 20 exhibits a maximum value centered at the dispersion region of $M'(\omega)$ (Fig. 19) and the peak positions increases with the incorporation of $Er_2O_3$ and $Yb_2O_3$ and approaches a low-frequency plateau, which is generally linked with the polarization effects of long-range hopping of mobile ions. Furthermore, in the hopping process, the more mobile cations ($Na^+$) may now displace across longer distances. As a result, we may deduce that charge carriers are restricted to potential wells that are mobile over small distances in the frequency area above $M''(\omega)$ peak maximum, whereas charge carriers are mobile over vast distances in the frequency region below $M''(\omega)$ peak maximum [78]. $M''(\omega)$ plots reveal a large conductivity relaxation peak for the distribution of free charge relaxation time, indicating a non-Debye model in the glass. The normalized plot of $M''/M''_{max}$ against log ($f/f_{max}$) of the modulus for NPZEr05Yb05 glass at different

**Fig. 17** The frequency dependence of $M'(\omega)$ at different temperatures for NPZ glass
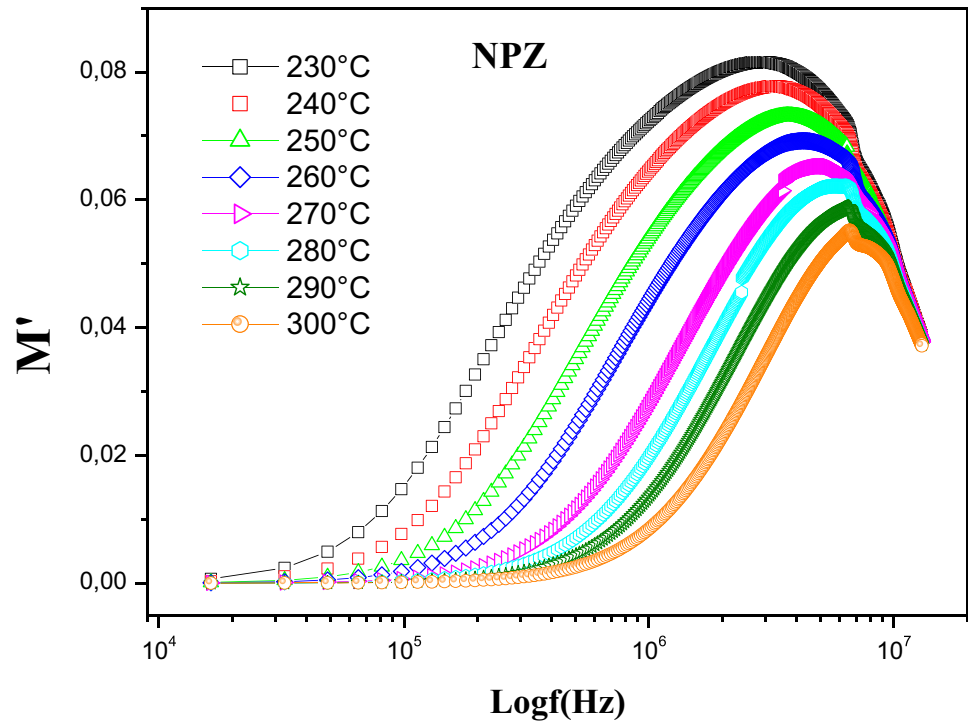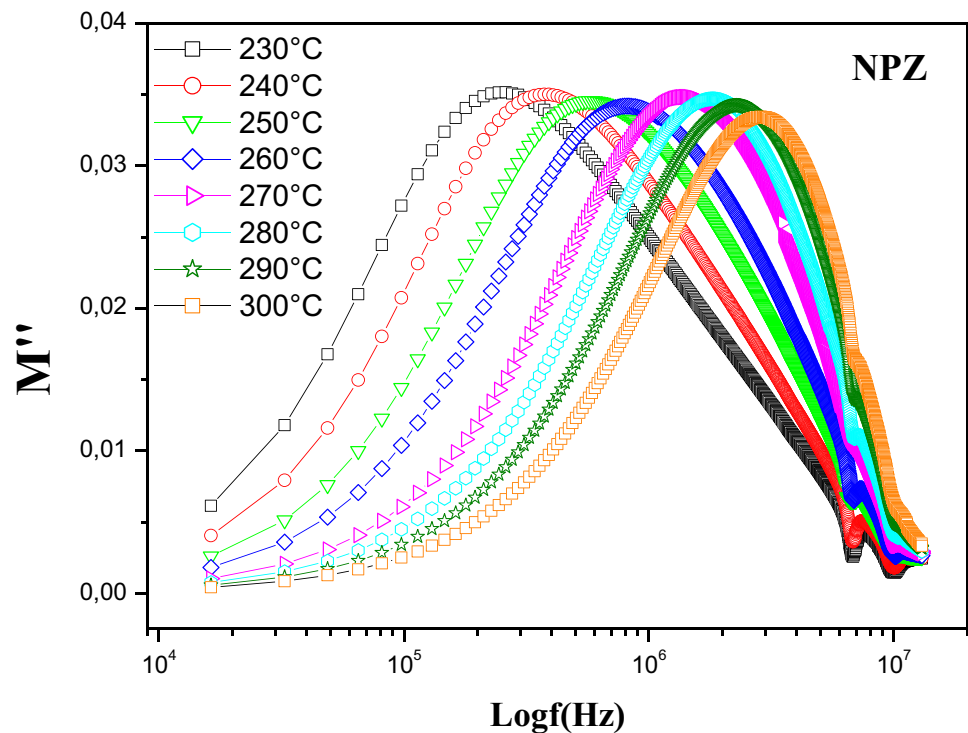


**Fig. 18** The frequency dependence of $M''(\omega)$ for NPZ glass at different temperatures



temperatures is shown in Fig. 21. The coincidence of the modulus curves for all temperatures suggests that these glasses have a common relaxation process for a certain range of temperatures that occur at various frequencies [52]. In Fig. 21, we show a time–temperature superposition indicating an unaltered conduction mechanism, as well as a wide peak attributed to the total of relaxations happening in bulk materials. This suggests a single ion transport mechanism that functions throughout the whole composition and temperature

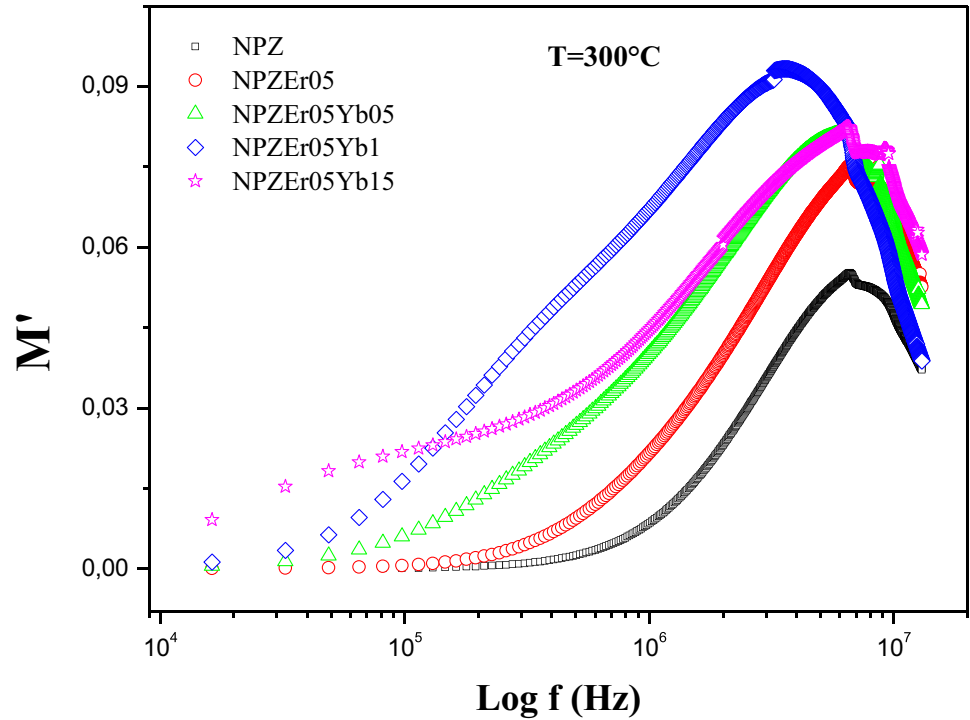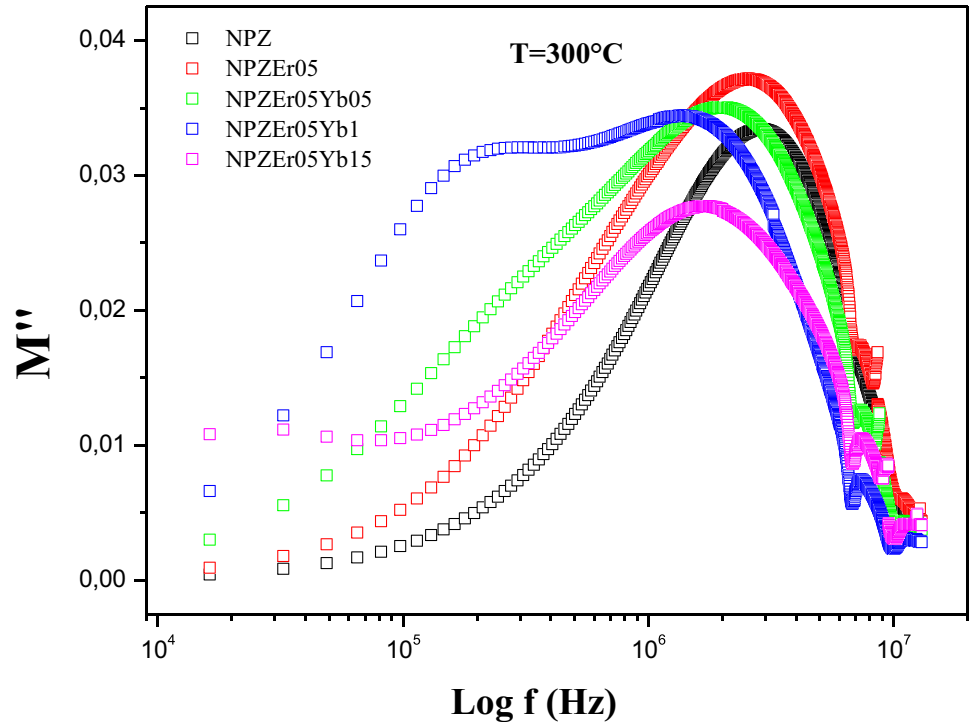**Fig. 19** The frequency dependence of M′(ω) at $T = 300$ °C for NPZ, NPZEr05, NPZEr05Yb05, NPZEr05Yb1, and NPZEr05Yb15 glasses



**Fig. 20** The frequency dependence of M″(ω) at $T = 300$ °C for NPZ, NPZEr05, NPZEr05Yb05, NPZEr05Yb1, and NPZEr05Yb15 glasses



range investigated. The comparison of impedance and electrical modulus data enables the assessment of bulk response in terms of localized, i.e., defect relaxation, or non-localized, i.e., ionic or electronic conductivity [79].

## Conclusions

Phosphate glasses containing $Er^{3+}$ and $Er^{3+}/Yb^{3+}$ were prepared via a melt quenching technique. The X-ray

**Fig. 21** Curves M″/M″max versus log (f /fmax), for NPZ-Er05Yb05 glass at different temperatures
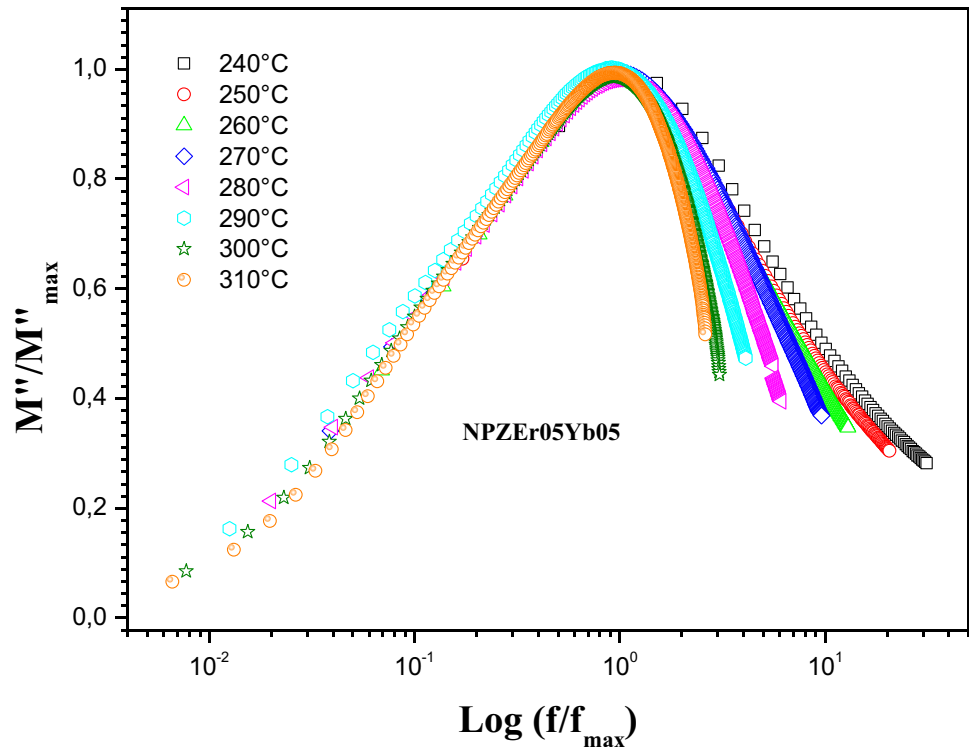


diffraction study confirmed the amorphous nature of these glass samples, whereas the appearance of significant peaks of the NPZEr05Yb15 glass sample confirms the existence of nanocrystallites. The stability of the produced glass samples is examined using differential scanning calorimetry (DSC). The addition of $Yb_2O_3$ to a glass matrix causes the phosphate glass network to depolymerize, confirming the $PO_4$ unit distortion. Temperature, glass composition, and the concentration of rare earth ions $(Er_2O_3/Yb_2O_3)$ influence the activation energy and dc conductivity. When $Yb_2O_3$ is raised from 0.5 to 1.5 mol%, the conductivity increases by two orders of magnitude. The structural alterations in the phosphate glass network are expected to cause such behavior. The ac conductivity has a strong temperature dependency, with observed values increasing with frequency and temperature. With the variation of log(f), both $\varepsilon'$ and $\varepsilon''$ as well as tan δ show somewhat identical behavior, where they show a steady decline with the growth of log(f). This drop as the frequency rises implies the presence of dipoles, which might be caused by a decrease in space charge carriers. As a result, the zinc phosphate glasses had greater dielectric constant values while having a lower loss. The dispersion of the relaxation time for mobile ions resulting from the variation in the random energy barriers is expressed by the non-Debye type in the modulus plot. Our manufactured glasses show a shift from ionic to electronic conduction, which might be useful in integrated micro-batteries.

# References

1. Soltani, I., Hraiech, S., Horchani-Naifer, K., Ferid, M.: Effects of silver nanoparticles on the enhancement of up conversion and infrared emission in Er3+/Yb3+ co-doped phosphate glasses. Opt. Mater. **77**, 161–169 (2018)
2. Soltani, I., Hraiech, S., Horchani-Naifer, K., Elhouichet, H., Gelloz, B., Ferid, M.: Thermal, structural and optical properties of Er3+ doped phosphate glasses containing silver nanoparticl. J. Alloy. Compd. **686**, 556–563 (2016)
3. Florez, A., Ulloa, E.M., Cabanzo, R.: Optical properties of Nd3+ and Er3+ ions in fluoro-phosphate glasses: Effects of P2O5 concentration and laser applications. J. Alloy. Compd. **488**, 606–611 (1990)
4. Knowles, J.C.: Phosphate based glasses for biomedical applications. J. Mater. Chem. **13**, 2395–2401 (2003)
5. Kabi, S., Ghosh, A.: Dynamics of Ag+ ions and immobile salt effect in CdI2 doped silver phosphate glasses. Solid State Ionics **187**, 39–42 (2011)
6. Shaw, A., Ghosh, A.: Correlation of microscopic length scales of ion dynamics with network structure in lithium-iodide–doped lithium metaphosphate glasses. EPL- Europhys. Lett. **100**(6), 0295–5075 (2012)
7. Shaw, A., Ghosh, A.: Influence of Immobile Ions on the Length Scale of Ion Transport in Conducting Phosphate Glasses. J. Phys. Chem. C. **116**, 24255–24261 (2012)
8. Ghosh, A.: Memory switching in bismuth-vanadate glasses. J. Appl. Phys. **64**, 2652 (1988)
9. Livage, J., Jollivet, J.P., Tronc, E.: Electronic Properties of Mixed Valence Oxide Gels. J. Non-Cryst. Solids. **121**, 35–39 (1990). https://doi.org/10.1016/0022-3093(90)90100-Z
10. Sakuri, Y., Yamaki, J.: V2O5-P2O5 glasses as cathode for lithium secondary battery. J. Electrochem. Soc. **132**, 512–513 (1985)
11. Krishna, M., Veeraiah, G.N., Venkatramaiah, N., Venkatesan, R.: Induced crystallization and physical properties of

Li2O–CaF2–P2O5: TiO2 glass system: part I. Characterization, spectroscopic and elastic properties. J. Alloy. Compd. **450**, 477–485 (2008)

12. Kundu, V., Dhiman, R.L., Maan, A.S., Goyal, D.R.: Structural and Physical Properties of $Fe_2O_3$-$B_2O_3$-$V_2O_5$ Glasses. Adv. Condens. Matter Phys. **937054**, 7 (2008)

13. Renuka, C., Sujatha, B., Sivasankarareddy, N., Viswanatha, R., Narayanareddy, C.: Conductivity studies on molybdo-phosphate glasses containing ZnO. AIP Conf. Proc. **1942**, 110039 (2018). https://doi.org/10.1063/1.5029022

14. Dyre, J.C., Maass, P., Roling, B., Sidebottom, D.L.: Fundamental questions relating to ion conduction in disordered solids. Rep. Prog. Phys. **72**, 046501 (2009)

15. Brow, R.K.: The structure of simple phosphate glasses. J. Non-Cryst. Solids **263–264**, 1–28 (2000)

16. Brow, R.K., Tallant, D.R., Hudges, J.J., Martin, S.W., Irwin, A.D.: The short-range structure of sodium ultraphosphate glasses. J. Non-Cryst. Solids. **177**, 221–228 (1994)

17. Choudhary, B.P.: Electrical and dielectric behavior of zinc phosphate glasses. Materials Today: Proceedings **4**, 5706–5714 (2017)

18. Soltani, I., Hraiech, S., Horchani-Naifer, K., Elhouichet, H., Ferid, M.: Effect of silver nanoparticles on spectroscopic properties of $Er^{3+}$ doped phosphate glass. Opt. Mater. **46**, 454–460 (2015)

19. Goel, A., Tulyaganov, D.U., Kharton, V.V., Yaremchenko, A.A., Ferreira, J.M.F.: The effect of $Cr_2O_3$ addition on crystallization and properties of $La_2O_3$-containing diopside glass-ceramics. Acta Mater. **56**, 3065–3076 (2008)

20. Khor, S.F., Talib, Z.A., Sidek, H.A.A., Daud, W.M., Ng, B.H.: Effects of ZnO on dielectric properties and electrical conductivity of ternary zinc magnesium phosphate glasses. Am. J. Applied Sci. **6**, 1010–1014 (2009)

21. Cullity, B.D.: Elements of X-ray Diffraction, Addison-Wesley metallurgy series. Reading, Mass: Addison-Wesley, Book. **904102259**, 1–167 (1956)

22. Sdiri, N., Elhouichet, H., Elakermi, E., Dhifallah, A., Ferid, M.: Structural investigation of amorphous $Na_2O$–$P_2O_5$–$B_2O_3$ correlated with its ionic conductivity. J. Non-Cryst. Solids. **409**, 34–42 (2015)

23. Sandhya Rani, P., Singh, R.: Electron spin resonance and magnetization studies of $ZnO$–$TeO_2$–$Fe_2O_3$ glasses. J. Phys. Chem. Solids. **74**, 338–343 (2013)

24. Cozar, O., Magdas, D.A., Nasdala, L., Ardelean, I., Damian, G.: Raman spectroscopic study of some lead phosphate glasses with tungsten ions. J. Non-Cryst. Solids **352**, 3121–3125 (2006)

25. Flambard, A., Videau, J.J., Delevoye, L., Cardinal, T., Labrugère, C., Rivero, C.A., Couzi, M., Montagne, L.: Structure and nonlinear optical properties of sodium–niobium phosphate glasses. J. Non-Cryst. Solids. **354**, 3540–3547 (2008)

26. Soltani, I., Hraiech, S., Horchani-Naifer, K., Massera, J., Petit, L., Ferid, M., Férid, M.: Thermal, structural and optical properties of $Er^{3+}$ doped phosphate glasses containing silver nanoparticles. J. Non-Cryst. Solids. **438**, 67–73 (2016)

27. Sułowska, J., Wacławska, I.: Structural role of Cu in the soil active glasses. Proc. Appl. Ceram. **6**, 77–82 (2012)

28. Karakassides, M.A., Saranti, A., Koutselas, I.: Preparation and structural study of binary phosphate glasses with high calcium and/or magnesium content. J. Non-Cryst. Solids. **347**, 69–79 (2004)

29. Mahfoudhi., M. (2019) $Eu^{3+}$ ion environment modification by Electron and femtosecond laser irradiation in metaphosphate and polyphosphate glasses., Physics [physics]. Université Paris Saclay (COmUE), English. ffNNT : 2019SACLX066ff. fftel-03227516.

30. Hameed, A.S.H., Karthikeyan, C., Ahamed, A.P., Thajuddin, N., Alharbi, N.S., Alharbi, S.A., Ravi, G.: In vitro antibacterial activity of ZnO and Nd doped ZnO nanoparticles against

31. ESBL producing Escherichia coli and Klebsiella pneumoniae. Sci. Rep. **6**, 24312 (2016)

31. Goel, S., Sinha, N., Yadav, H., Joseph, A.J., Kuma, B.: Experimental investigation on the structural, dielectric, ferroelectric and piezoelectric properties of La doped ZnO nanoparticles and their application in dye-sensitized. Physica E. **91**, 72–81 (2017)

32. Farhadi NH, Rosli MR, Kimpa MI, Esa F, Ismail MH, Mayzan MZH M Synthesis and Properties of Zinc Iron Phosphate Glasses Prepared by Microwave and Conventional Processing Methods. J Sci Tech 9:87–91

33. Jermoumi, T., Hassan, S., Hafid, M.: Structural investigation of vitreous barium zinc mixed. Metaphosphate, Vib Spect **32**, 207–213 (2003)

34. Darwishab, A.A.A., El-Zaidiac, E.F.M., El-Nahassc, M.M., Hanafybd, T.A., Al-Zubaidib, A.A.: Dielectric and electrical conductivity studies of bulk lead (II) oxide (PbO). J. Alloy Compd. **589**, 393–398 (2014)

35. Sdiri, N., Elhouichet, H., Azeza, B., Mokhtar, F.: Studies of (90–x) $P_2O_5$x$B_2O_3$10$Fe_2O_3$ glasses by Mossbauer effect and impedance spectroscopy methods. J. Non-Cryst. Solids. **371–372**, 22–27 (2013)

36. Jlassi, I., Sdiri, N., Elhouichet, H., Ferid, M.: Raman and impedance spectroscopy methods of P2O5-Li2O- $Al_2O_3$ glass system doped with MgO. J. Alloys Compd. **645**, 125–130 (2015)

37. Choudhary, B.P.: Optimization of electrical conductivity in copper phosphate glasses. Mater. Today: Proceedings **29**, 1235–1238 (2020)

38. Tiliakos, A., Iordache, M., Marinoiu, A.: Ionic Conductivity and Dielectric Relaxation of NASICON Superionic Conductors at the Near-Cryogenic Regime. Appl. Sci. **11**, 8432 (2021)

39. Bhide, A., Hariharan, K.: Sodium ion transport in $NaPO_3$–$Na_2SO_4$ glasses. Mat. Chem. Phys. **105**, 213–221 (2007)

40. Friesen, G., Ozsar, M.E., Dunlop, E.: Impedance model for CdTe solar cells exhibiting constant phase element behaviour. Thin Solid Films **361–362**, 303–308 (2000)

41. Jorcin, J.B., Orazem, M.E., Pébère, N., Tribollet, B.: CPE analysis by local electrochemical impedance spectroscopy. Electrochim. Acta **51**, 1473–1479 (2006)

42. Barde, R.V., Nemad, K.R., Waghuley, S.A.: AC conductivity and dielectric relaxation in V2O5–P2O5–$B_2O_3$ glasses. J. Asian Ceram. Soc. **3**, 116–122 (2015)

43. Affleck, L., Leach, C.: Microstructures of $BaTiO_3$ based PTC thermistors with Ca, Sr and Pb additions. J. Eur. Ceram. Soc. **25**, 3017–3020 (2005)

44. Murawski, L., Barczynski, R.J.: Electronic and ionic relaxations in oxide glasses. Solid State Ionics **176**, 2145–2151 (2005)

45. Pant, M., Kanchan, D.K., Gondaliya, N.: Transport properties and relaxation studies in BaO substituted Ag2O–V2O5–TeO2 glass system. Mater Chem Phys **115**, 98–104 (2009)

46. Sundarakannan, B., Kakimoto, K., Ohsato, H.: Frequency and temperature dependent dielectric and conductivity behavior of $KNbO_3$ ceramics. J. Appl. Phys. **94**, 5182–5187 (2003)

47. Yassin AY, Raouf Mohamed A, Abdelghany AM, Abdelrazek EM (2018) Enhancement of dielectric properties and AC electrical conductivity of nanocomposite using poly (vinyl chloride-co-vinyl acetate-co-2-hydroxypropyl acrylate) filled with graphene oxide. J Mater Sci Mater Elec. https://doi.org/10.1007/s10854-018-9679-7

48. Salman, F.: AC conductivity and Dielectric Study of Chalcogenide glasses of Se-Te-Ge System. Turk J Phys **28**, 41–48 (2004)

49. Mottn NF, Davis EA (1979) International series of monographs on physics. Electron. Processes Non-Cryst.Mater, Oxford : Clarendon Press; New York : Oxford University Press, 7, 157–164

50. Anand, G., Kuchhal, P., Sarah, P.: AC and DC Conductivity Studies on Lead-Free Ceramics:Sr1–xCaxBi4Ti4O15(x¼40, 0.2, 0.4, 0.6, 0.8). Part. Sci. Tech **33**, 41–46 (2015)

51. James, A.R., Srinivas, K.: Low temperature fabrication and impedance spectroscopy of PMN-PT ceramics. Mat. Res. Bul. **34**, 1301–1310 (1999)

52. Tabib, A., Sdiri, N., Elhouichet, H., Férid, M.: Investigations on electrical conductivity and dielectric properties of Na doped ZnO synthesized from sol gel method. J. Alloy. Compd. **S0925–8388**, 02512–02522 (2015)

53. Saad, M., Stambouli, W., Sdiri, N., Elhouichet, H.: Effect of mixed sodium and vanadium on the electric and dielectric properties of zinc phosphate glass. Mat. Res. Bul. **89**, 224–231 (2017)

54. Elliott, S.R.: Ac conduction in amorphous chalcogenide and pnictide semiconductors. Adv. Phys. **36**, 135 (1987)

55. Fayek, M.K., Mostafa, M.F., Sayedahmed, F., AtaAllah, S.S., Kaiser, M.: On the electrical behavior of nickel ferrite-gallates. J. Magn. Magn Mater **210**, 189–195 (2000)

56. Anjali, Patial, B.S., Bhardwaj, S., Awasthi, A.M., Thakur, N.: On the AC-conductivity mechanism in nano-crystalline Se79−xTe15In6Pbx (x= 0, 1, 2, 4, 6, 8 and 10) alloys. Physica B: Cond. Mat. **523**, 52–61 (2017)

57. Long, A.R.: Frequency-dependent loss in amorphous semiconductors. Adv. Phys. **31**, 553–637 (1982)

58. Aziz, S.B., Abdullah, O., Saeed, S.R., Ahmed, H.M.: Electrical and dielectric properties of copper ion conducting solid polymer electrolytes based on chitosan: CBH model for ion transport mechanism. Int J. Electrochem. Sci. **13**, 3812–3826 (2018)

59. Barranco, A.P., Amador, G., Huanosta, M.P.A., Valenzuela, R.: Phase transitions in ferrimagnetic and ferroelectric ceramics by ac measurements. Appl. Phys. Lett. **73**, 2039–2041 (1998)

60. Mauritz, K.A.: Dielectric relaxation studies of ion motions in electrolyte-containing perfluorosulfonate ionomers. 4. Long-range ion transport. Macromol. **22**, 4483–4488 (1989)

61. Poloju, M., Jayababu, N., Manikandan, E., Reddy, M.V.R.: Enhancement of the isopropanol gas sensing performance of SnO 2/ZnO core/shell nanocomposites. J. Mat. Chem. C. **5**, 2662–2668 (2017)

62. Garbarczyk, J.E., Machowski, P., Wasiucionek, M., Tykarski, L., Bacewicz, R., Aleksiejuk, A.: Studies of silver–vanadate–phosphate glasses by Raman, EPR and impedance spectroscopy methods. J. Solid State Ionics. **136**, 1077–1083 (2000)

63. Gedam, R.S., Ramteke, D.D.: Electrical, dielectric and optical properties of La2O3 doped lithium borate glasses. J. Phys. Chem. Solids. **4**, 1039–1044 (2013)

64. Khor, S.F., Talib, Z.A., Sidek, H.A.A., Daud, W.M., Ng, Am., B.H.: Effects of ZnO on dielectric properties and electrical conductivity of ternary zinc magnesium phosphate glasses. J. Applied Sci. **6**(5), 1010–1014 (2009)

65. Zaafouri, A., Megdiche, M., Gargouri, M.: AC conductivity and dielectric behavior in lithium and sodium diphosphate LiNa3P$_2$O$_7$. J. Alloy. Compd. **584**, 152–158 (2014)

66. Barde, R.V., Waghuley, S.A.: Study of AC electrical properties of V$_2$O$_5$–P$_2$O$_5$–B$_2$O$_3$–Dy$_2$O$_3$ glasses. J Ceramint. **39**, 6303–6311 (2013)

67. Badapanda, T., Senthil, V., Rout, S.K., Cavalcante, L.S., Simoes, A.Z., Sinha, T.P., de Jesus, M.M., Longo, E., Varela, J.A.: Rietveld refinement, microstructure, conductivity and impedance properties of Ba [Zr0. 25Ti0. 75] O$_3$ ceramic. Curr. Appl. Phys. **11**, 1282–1293 (2011)

68. Srilatha, K., SambasivaRao, K., Gandhi, Y., Ravikumar, V., Veeraiah, N.: Fe concentration dependent transport properties of LiI–AgI–B$_2$O$_3$ glass system. J. Alloy. Comp. **507**, 391–398 (2010)

69. Choudhary, B.P., Rai, S., Singh, N.B.: Properties of silver phosphate glass doped with nanosize zinc oxide. Ceram. Inter. **42**, 10813–10825 (2016)

70. Langar, A., Sdiri, N., Elhouichet, H., Ferid, M.: Conductivity and dielectric behavior of NaPO3–ZnO–V2O5 glasses. J. Alloy. Compd. **590**, 380–387 (2014)

71. Charles, J.B., Ganam, F.D.: Dielectric studies on sodium fluoroantimonate single crystals. *Cryst. Res. Technol.* **29**, 707–712 (1994)

72. Hajra, S., Sahu, M., Purohit, V., Choudhary, R.N.P.: Dielectric, conductivity and ferroelectric properties of lead-free electronic ceramic:0.6Bi(Fe0.98Ga0.02)O3–0.4BaTiO3. Heliyon **5**, 01654 (2019)

73. ElBellihi, A.A., Bayoumy, W.A., Masoud, E.M., Mousa, M.A.: Preparation, Characterizations and Conductivity of Composite Polymer Electrolytes Based on PEO-LiClO4 and Nano ZnO Filler. Bull. Korean Chem. Soc. **33**, 2949–3295 (2012)

74. Kanagathara, N., Renganathan, N.G., Marchewka, M.K., Sivakumar, N., Gayathri, K., Krishnan, P., Gunasekaran, S., Anbalagan, G.: FT-IR, FT-Raman spectra and DFT calculations of melaminium perchlorate monohydrate. Spectrochim. Acta A. **101**, 112–118 (2013)

75. Angell, C.A., Ngai, K.L., McKenna, G.B., McMillan, P.F., and. Martin, S.W.: Relaxation in glass forming liquids and amorphous solids. J. Appl. Phys. **88**(6), 3113–3157 (2000)

76. Ben Rhaiem, A., Hlel, F., Guidara, K., Gargouri, M.: Dielectric relaxation and ionic conductivity studies of [N(CH 3 ) 4 ] 2Cu 0.5Zn 0.5Cl 4. J. Alloy. Comp. **463**, 440–445 (2008)

77. Nawar, A.M., Abd El-Khalek, H.M., El-Nahass, M.M.: Dielectric and Electric Modulus Studies on Ni (II) Tetraphenyl Porphyrin Thin Films. Org. Opto-Elect. **1**, 25–38 (2015)

78. Dutta, A., Sinha, T.P., Jena, P., Adak, S.: Ac Conductivity and Dielectric Relaxation in Ionically Conducting Soda-Lime–Silicate Glasses. J. Non-Cryst Solids. **354**, 3952–3957 (2008)

79. Gerhardt, R.: Impedance and dielectric spectroscopy revisited: Distinguishing localized relaxation from long-range conductivity. J. Phys. Chem. Solids. **55**, 1491–1506 (1994)